PRISM: Multiplexed Profiling of RNA In-Situ through Single-round of Imaging in Three-Dimensional Tissue

Tianyi Chang,[1,#] Shihui Zhao,[1,#] Kunyue Deng,[1,2,#] Zhizhao Liao,[1,3,#] Mingchuan Tang,[1,4,#] Yanxi Zhu,[1] Wuji Han,[1,4] Chenxi Yu,[1] Wenyi Fan,[1] Mengcheng Jiang,[1] Guanbo Wang,[1,3,5] Dongfang Liu,[6] Jirun Peng,[6,7] Yuhong Pang,[1] Peng Fei,[8] Jianbin Wang,[3,9] Chunhong Zheng,[1,10,11,*] and Yanyi Huang[1,2,3,5,*]

[1] Biomedical Pioneering Innovation Center (BIOPIC), Peking University International Cancer Institute, School of Life Sciences, Peking-Tsinghua Center for Life Sciences, Academy for Advanced Interdisciplinary Studies, Peking University, Beijing 100871, China
[2] College of Chemistry and Molecular Engineering, Beijing National Laboratory for Molecular Sciences, Peking University, Beijing 100871, China
[3] Changping Laboratory, Yard 28, Science Park Rd., Changping District, Beijing, China
[4] Yuanpei College, Peking University, Beijing 100871, China
[5] Institute for Cell Analysis, Shenzhen Bay Laboratory, Shenzhen 518132, China
[6] Department of Surgery, Beijing Shijitan Hospital, Capital Medical University, Beijing 100038, China
[7] Ninth School of Clinical Medicine, Peking University, Beijing 100038, China
[8] School of Optical and Electronic Information – Wuhan National Laboratory for Optoelectronics, Huazhong University of Science and Technology, Wuhan 430074, China
[9] School of Life Sciences, Tsinghua University, Beijing 100084, China
[10] Key Laboratory of Carcinogenesis and Translational Research (Ministry of Education/Beijing), Peking University Cancer Hospital & Institute, Beijing 100142, China
[11] State Key Laboratory of Molecular Oncology, Peking University Health Science Center, Beijing 100191, China.

[#] These authors contributed equally to this work.
* Correspondance should be addressed to chunhong_zheng@bjmu.edu.cn (C.Z.) and yanyi@pku.edu.cn (Y.H.)

Abstract

To resolve many RNA species in situ, cyclic reactions are typically necessary to increase the multiplexity since conventional fluorescence microscopy is often limited to five channels. Therefore, sophisticated instrumentation is needed to perform in-situ sequencing or sequential fluorescence in-situ hybridization imaging, restricting the widespread adoption of spatial RNA imaging methods among biological research communities. Here, we present 'Profiling of RNA In-situ through Single-round of iMaging' (PRISM), which leverages the spectral intensity levels to expand the coding capacity. With a radius vector coding strategy to ensure the orthogonality of codewords, PRISM can reach up to 64-plex RNA imaging in a single imaging shot with conventional microscopes. As a panel-based spatial transcriptomic imaging approach, the entire experimental process can be completed within one day. We verified PRISM's versatility on various tissues, such as mouse brains, mouse embryos, and human hepatocellular carcinoma (HCC) samples, generating more than 5.7 million annotated cells. We performed quasi-3D spatial landscapes to track major cell types in different organs during embryonic development from E12.5 to E14.5. We also revealed the critical role of cancer-associated fibroblasts (CAFs) on immune infiltration and immune response heterogeneity within and between tumor microenvironments. We extended PRISM to 100-μm thick mouse brain slices to generate accurate 3D cell atlas and subcellular RNA localization landscapes. PRISM is robust and easy to operate, with a fast turnaround time and sub-cellular resolution, offering a new transcriptomic imaging toolbox for all biologists.

Introduction

The spatial arrangement of RNA transcripts is vital for unveiling biological interactions at the cellular or sub-cellular levels, exposing the diverse heterogeneity and structural compositions across various tissues. While numerous spatial transcriptomics technologies rely on surface-barcoded RNA capture and high-throughput sequencing[1–17], imaging-based methodologies, notably in-situ hybridization (ISH)[18–35] or in-situ sequencing (ISS)[36–56], offer a superior spatial resolution, enabling single-molecule detectability. It is highly demanded that the positions and quantities of multiple RNA transcript species within tissue samples be analyzed simultaneously. However, enhancing multiplexity typically involves conducting several rounds of labeling-stripping reactions or incorporating additional fluorescence channels.

Cyclic staining-imaging methods can efficiently code more transcript species using a finite number of fluorescence channels but often depend on sophisticated, delicate equipment that combines fluidics, optics, and temperature regulation. The lack of proper hardware has limited the widespread adoption of such methods, which are generally expensive and time-intensive. Precise signal spot registration across reaction cycles is challenging due to unavoidable sample deformation or displacement over extended experiment durations. Furthermore, slow reagent diffusion and exchange in thick tissues complicate three-dimensional RNA profiling, lengthening the time required for multiple reaction rounds and adding to spatial alignment difficulties.

Expanding the number of optical channels poses challenges, as spectral overlap may lead to signal crosstalk between channels, complicating signal deduction across different staining and imaging cycles. While certain strategies employ advanced microscopy techniques, such as super-resolution[20], fluorescence lifetime[29], or coherent Raman scattering microscopies[57], to identify more molecular species beyond traditional optical limits[35], the requirement for specialized equipment hinders the widespread applications of these methods in many biological laboratories. Despite using fluorescence intensity[40] as a coding strategy may increase multiplexity, the outcomes have often been disappointing due to marginal throughput enhancements and complex decoding procedures.

Here we present PRISM (**P**rofiling of **R**NA **I**n-situ through **S**ingle-round i**M**aging), a method that employs a radius vector code to distinguish dozens of RNA transcript species in large-scale tissues with sub-micron resolution through a single staining and imaging cycle. The entire experimental workflow, from sample preparation to data acquisition, can be completed within a day using common bench-top equipment and a conventional fluorescent microscope. We tested PRISM in various tissue samples, including mouse brains, mouse embryos and human hepatocellular carcinoma (HCC) samples. Employing a 30-gene panel, we developed a 3D cell atlas of mouse embryos at developmental stages E12.5, 13.5, and 14.5, comprising over 4.2 million cells categorized into 12 types, showcasing cellular compositions and organizations in different organs at various developmental phases. Additionally, using a 31-gene panel on 20 consecutive sections from an HBV-positive patient, we created a quasi-3D HCC tumor-normal transition landscape with approximately 1.4 million annotated cells across 34 cell types, uncovering the tumor microenvironment's heterogeneities at cellular resolution and demonstrating how cancer-associated fibroblasts (CAFs) construct a physical barrier against immune infiltration. PRISM's compatibility with intact 3D imaging was further validated using 100-μm-thick mouse brain slices, where a 30-gene panel effectively identified over 20 cell types within the cortex, hippocampus, thalamus, and hypothalamus regions through a single staining round using conventional confocal microscopy.

PRISM demonstrates that radius vector coding is a robust and feasible approach for multiplex RNA transcript in-situ imaging in tissues, utilizing only standard laboratory equipment.

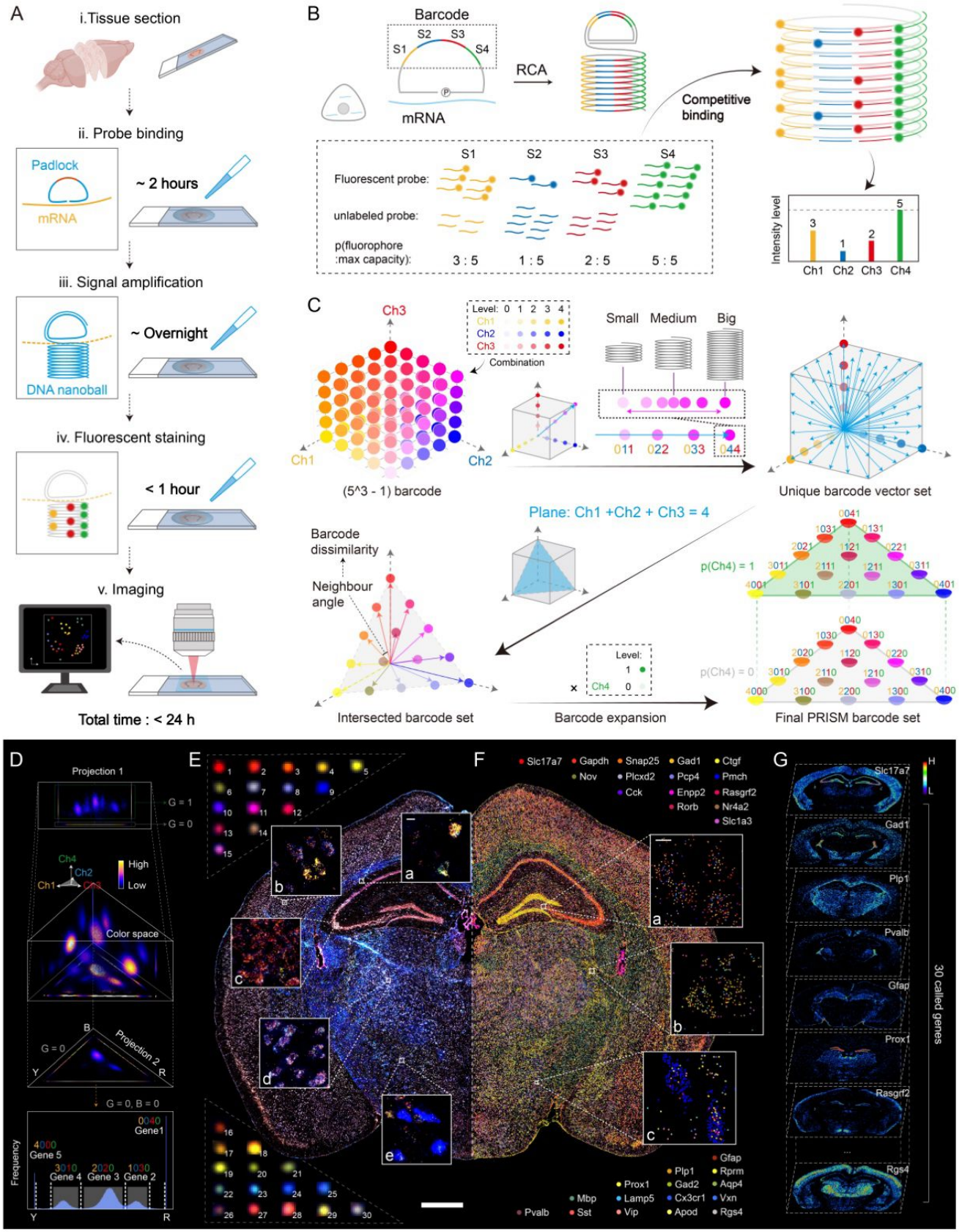

Fig. 1. Workflow and principle of PRISM encoding. (A) Workflow of PRISM experiment. The experiment started with a section of mouse brain tissue. Major steps include padlock probe binding, signal amplification (probe ligation and rolling circle amplification), fluorescent staining, and imaging. The entire experiment can be completed in 24 hours. **(B)** The intensity-level division is achieved by competitive binding to the target segment between fluorophore-labeled probes and unlabeled ones. Each segment, characterized

by a specific intensity level and spectral channel, poses a unique sequence capable of binding with corresponding probes. The mixing ratio for each probe pair corresponds to the designed ratio, ensuring that only the intended proportion of fluorophore binds to each segment. **(C)** Radius vector coding. Barcode candidates result from combinations of intensity levels and spectral channels. Due to the amplicon size heterogeneity in the experiment, the absolute signal intensity varies, causing the spot from a certain barcode to move along its radial ray in the color space. Therefore, all barcodes were considered their radius vector, forming a unique set of barcode vectors. Barcode vectors with small neighbor angles cannot be well distinguished. To maximize the dispersion of vectors, the barcode set intersected by plane (Ch1 + Ch2 + Ch3 = K) was adopted. Quantizing three channels into quarters and setting K to 4 allows for the generation of 15 barcodes. With a compromise Ch4 (which can't be quantized to many levels due to issues such as tissue autofluorescence) divided into 0 (no) or 1 (yes), the Total available barcodes are 30 or 31 (including only Ch4 itself). **(D)** Gene decoding in color space. The signals from four colors were converted into three-dimensional coordinates, and each spot was plotted in a "color space." 30 clusters located in different positions, each representing a unique barcode. Each barcode was identified by its specific location within the color space. **(E)** Spots in the raw image corresponded to 30 different barcodes. Each spot consists of four channels, shown within the same dynamic range. Scale bar: 10 μm, zoom-in image; 1 mm, below. **(F)** Decoded genes. Each gene was assigned a pseudo-color corresponding to its barcode. Scale bar: 10 μm. **(G)** Spatial distribution of 30 decoded genes.

Coding principles of PRISM

The PRISM protocol can be completed within a day, from sample preparation to imaging (Fig. 1A). It begins with hybridizing targeted gene transcripts using barcoded padlock probes, amplified locally into clones via rolling circle amplification[54]. The barcodes on these probes are segmented, with each segment corresponding to a spectral channel through hybridization with secondary fluorescent oligonucleotide probes. A color space is created from the spectral combinations of the fluorophores when the fluorescence intensity is taken into account, greatly expanding the encoding capacity. Each spectral channel is assigned several intensity levels. This is achieved via mixing fluorescent labeled and unlabeled secondary probes at specific ratios, which yields discrete signal because of the two type of secondary probes binding competitively during staining (Fig. 1B). For example, with three spectral channels, each channel is quantized into quarters (0, 1/4, 2/4, 3/4, 4/4), conceptually, one can write down the codes with 3-digit quinary numbers and encode $5^3 - 1 = 124$ genes.

However, in practice, the number of usable barcodes is reduced due to several factors. Some spectral ranges are unsuitable for ratio-intensity coding due to autofluorescence interference, which obscures the signal if too many intensity levels are used. Common fluorophores such as Texas Red (TR, Ch1), Alexa Fluor 488 (AF488, Ch2), Cy5 (Ch3), and Cy3 (Ch4) were chosen due to their widespread availability. Practically, certain channels may have to compromise to a fewer quantization divisions. For example, our experiments often found the Cy3 channel (Ch4) was a compromised channel due to the tissue autofluorescence. Additionally, variations in the sizes of amplified nanoballs can make some codes indistinguishable in spectral color space. For instance, a small amplicon barcoded (020) will not be able to separate from a twice-size amplicon barcoded (010), nor will it be (033) and (022). This is because the signal spot will move along the radial ray in the color space due to the variations in amplification size. To better describe the discriminability of barcodes under this circumstance, each barcode was conceptualized as a corresponding 'radius vector' in the color space, and only angularly distinct barcode vectors were considered legitimate (Fig. 1C, Fig. S1). To ensure ample dispersion of barcode vectors, we chose the plane (Ch1+Ch2+Ch3 = 4) in the coding space as the constraint; that is, the sum of the intensities of three quantized channels should be a constant 4. This way, we reach an optimal differentiability of intersected barcodes by calculating the angles between any two barcode vectors and eliminating the crosstalk between barcodes. As a result, with three quarterly quantized channels, we can obtain 15 barcodes, and if we include the Ch4 [either yes (1) or no (0)], the coding capacity can be doubled to 30. In addition, Ch4 can serve solely as a barcode, making the total barcode number 31.

Using conventional setups and a single round of staining operation, we performed cell typing on a 10-μm mouse brain coronal section with a 30-gene panel (Fig. 1D-F). The fluorescent puncta were

processed to dissect the ratio code of each amplicon and revealed the barcode of each transcript in situ (Fig. S2). All the barcodes were formed into 30 distinct clusters in the color space, faithfully recapturing the original design. The clusters were identified through manually adjustable Gaussian fitting probability prediction, with more than 80% spot-preserving efficiency (Fig. 1D, Fig. S3).

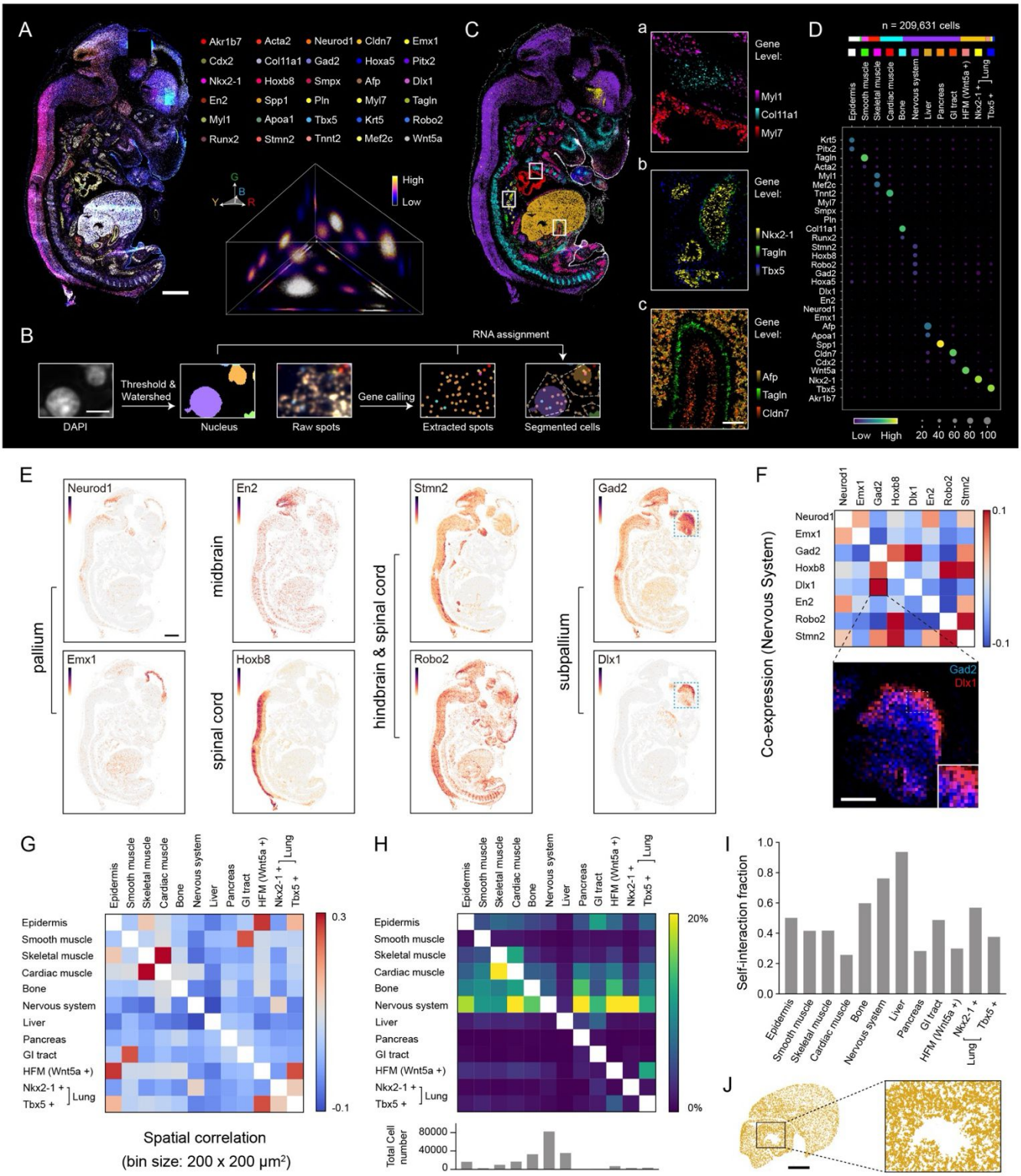

Fig. 2. Spatial profiling of mouse E13.5 embryo by PRISM. (A) A composite raw image of four channels of the mouse embryo E13.5 (sagittal section) by PRISM and the distribution of 30 clusters of spots in color space. Scale bar: 1mm. **(B)** Cell segmentation. Cells were segmented through a DAPI image, and each identified gene spot was assigned to the nearest nucleus through Euclidean distance. Scale bar: 5 μm. **(C)** Annotated cell type distribution of the mouse embryo. Cell type was determined by the most abundant gene within each cell. Zoom-in figs (a-c) were colored based on gene abundance. Scale bar: 100 μm. **(D)** Dot plot of each cell type. **(E)** Heterogeneity in the nervous system can be revealed through gene expression patterns. The cells were colored based on the abundance of their respective gene expressions and grouped according to the organ's location. Scale bar: 1 mm. **(F)** Co-expression

analysis revealed the developmental role of transcription factor DLX1 in forebrain GABAergic-neuron. Scale bar: 500 μm. **(G)** Coarse-grain spatial correlation analysis between general cell types. The spatial binning size is 200 x 200 μm^2. **(H)** Direct intercellular interaction between general cell types. The interaction degree was defined as the proportion of cells directly adjacent to another cell. The figure below shows the total cell number of each general cell type. **(I)** Direct intercellular interaction between each cell type itself. **(J)** Spatial distribution of liver cells. The zoom-in image shows numerous structures of hepatic lobes, each composed of several liver cells. Scale bar: 500 μm.

Mapping each barcode back into the sample allows for a submicron-resolution spatial distribution plot of 30 genes, with their patterns well correlated with RNA FISH results from Allen Brain Atlas (Fig. 1G, Fig. S4,5). The decoding accuracy was 94.6% by checking the overlap rate of strip-rehybridization experiments (Fig. S6). Cell segmentation and typing were done by integrating 30 RNA spatial images with DAPI-stained nuclei territories (Fig. S7). In this brain section, we identified 71,435 cells in total, with 5 major types including excitatory neurons (39,757, 55.6%), inhibitory neurons (13,134, 18.4%), and non-neuronal cells (oligodendrocytes, 8,244, 11.5%; astrocytes, 7,062, 9.9%; microglia cells, 3,238, 4.5%). Further differentiating these cells into subtypes clearly showed the architectural organizations of the mouse brain at the single-cell resolution (Fig. S8).

Spatial profiling of mouse embryos reveals developmental intracellular interaction

We utilized PRISM with a specific panel of 30 marker genes to explore the intricate structural dynamics and cellular interactions within various tissues and organs during embryonic development (Fig. 2A-D, Fig. S9-11). A 10-μm whole-mount section of an E13.5 mouse embryo revealed 12 primary cell types, including the epidermis, bone, and gastrointestinal tract, distinguished by the most abundantly expressed genes (Fig. 2C,D). Notably, the nervous system, constituting 39.3% of the total cell count, can be further classified based on marker gene expression, revealing spatial organization within the embryonic brain at E13.5, spanning the forebrain (pallium, subpallium), midbrain, hindbrain, and spinal cord (Fig. 2E). Gene co-expression analyses were conducted to determine the co-localization of genes within the nervous system (Fig. 2F), with significant co-localization observed for *Hoxb8*, *Robo2*, and *Stmn2* in the spinal cord region. Additionally, the co-presence of *Gad2* and *Dlx1* in the subpallium supported the hypothesis that DLX1 transcription factors directly influence *Gad2* expression, a crucial interaction for the development of GABAergic neurons in the forebrain and illustrated a key aspect of neuronal differentiation and specialization.

A coarse-grained spatial correlation analysis was performed to understand the relationship between various cell types across tissue locations (Fig. 2G, Fig. S12). The co-occurrence of skeletal and cardiac muscle cells, as well as GI tract and smooth muscle cells, indicates their collaborative roles in specific developmental functions. Both *Wnt5a*$^+$ and *Tbx5*$^+$ cells play critical roles in coordinating limb development. In our analysis, *Wnt5a*$^+$ Limb mesenchymal cells are primarily distributed in the distal regions of the limb and the terminal mouth area but spatially proximal to epidermis cells. Additionally, *Tbx5*$^+$ limb fibroblasts demonstrate a high spatial correlation with *Wnt5a*$^+$ cells. They exhibit a greater abundance in the limb and are primarily distributed in the proximal regions, exemplifying their joint contribution to the formation and functioning of the limbs.

The further refined analysis assessed direct intercellular interactions (Fig. 2H), revealing a complex network of developmental interactions between the nervous system and other organs at E13.5. Notably, pancreatic cells marked by *Spp1* exhibited significant interactions with chondrocytes and osteoblasts. The presence of islands of *Spp1*$^+$ cells within the skeletal structure suggests their possible involvement in the early formation of the intervertebral disc[58] (Fig. S13). The previously

noted spatial correlation between *Wnt5a*$^+$ and *Tbx5*$^+$ cells was confirmed to be a direct interaction. Additionally, *Nkx2-1*$^+$ cells, highly expressed in certain neural precursors[59], were found predominantly in the subpallium and demonstrated extensive interactions with the nervous system, including the spinal cord. Remarkably, numerous *Nkx2-1*$^+$ cell clusters, with their distinctive disk-like structure, are scattered across the alar plates of the spinal cord, suggesting a role in cell differentiation and migration within the spinal cord (Fig. S13). Not surprisingly, interactions within the same cell type are considerable (Fig. 2I). Particularly, 94% of hepatocytes interact with each other in close proximity (Fig. 2J), indicating early multicellular structure formation within the hepatic lobe and the establishment of basic hepatic architecture by E13.5.

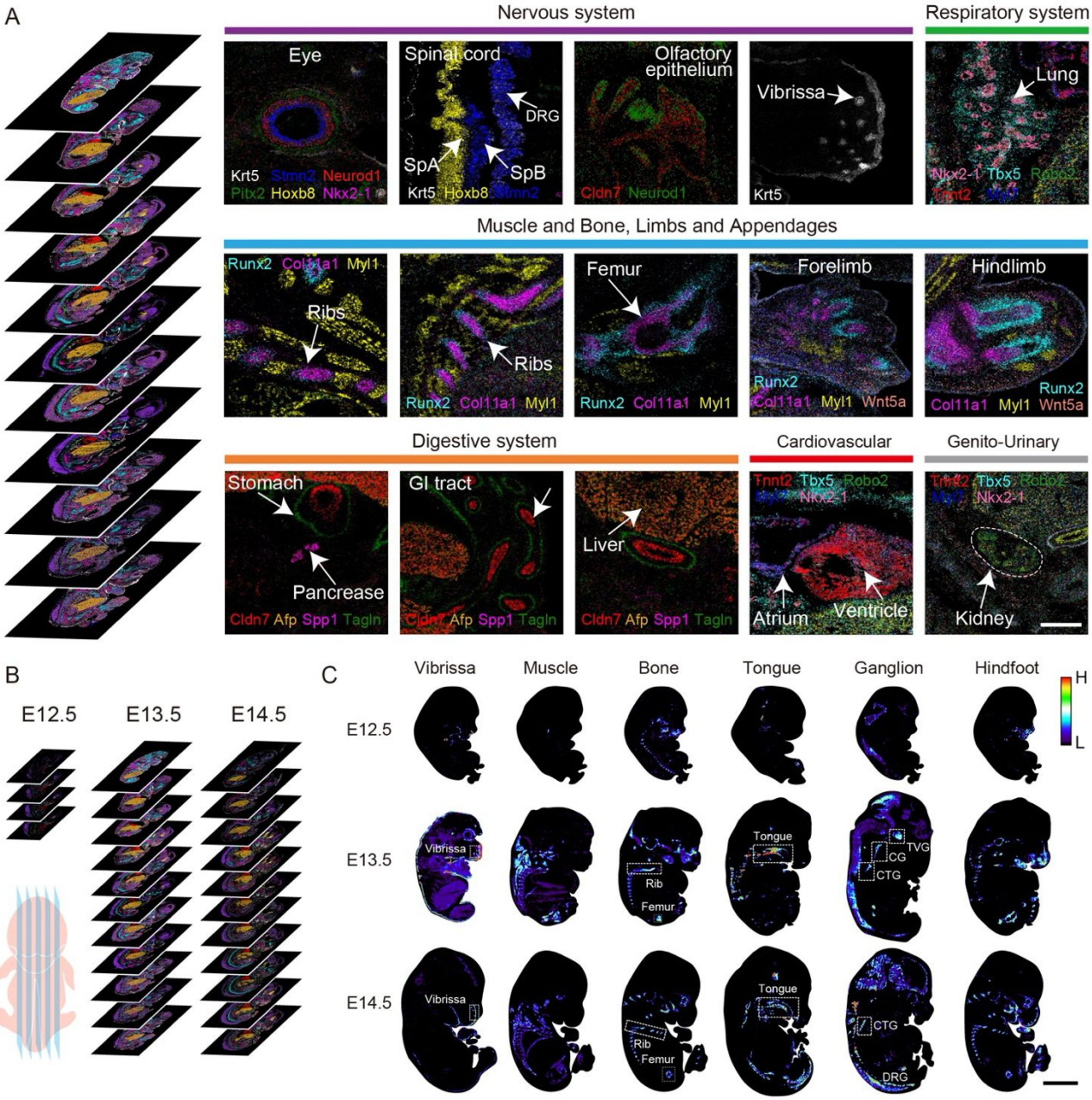

Fig. 3. High-throughput spatial profiling of mouse embryos E12.5, E13.5, and E14.5. (A) Developmental structures across different systems from a sampled-3D spatial atlas of the E13.5 embryo, constructed from 11 sagittal sections at an average interval of 280 μm. Fine structures from the nervous, respiratory, motion, digestive, cardiovascular, and genitourinary systems are collected from different sections. Cells within these structures are colored based on the abundance of their respective marker genes. Scale bar: 500 μm. **(B)** Sampled-3D spatial atlas of E12.5 (4 sections), E13.5 (11 sections) and E14.5 (11 sections) embryo. **(C)** Developmental progression at different stages is revealed by annotated cell distribution. DRG (Dorsal Root Ganglion); CG (Cervical ganglion); TVG (Trigeminal V ganglion); CTG (Cervico thoracic ganglion). Scale bar: 2.5 mm.

Spatial-temporal atlases illustrate embryonic organ development

Single-round 30-plex imaging has enabled rapid spatial profiling on a large scale. We created a sampled 3D cell atlas of an E13.5 mouse, utilizing 11 whole-mount sections spaced 280 μm apart, capturing a total of 2,331,513 annotated cells (Fig. 3A). This comprehensive experiment, from sample preparation to imaging, was completed within three days to generate an annotated cell atlas, allowing for the visualization of various early developmental structures.

At the E13.5 stage, the nervous system showcases distinct structures such as the multi-layered composition of the eye (marked by *Neurod1*$^+$, *Pitx2*$^+$, *Stmn2*$^+$), the spinal cord's alar and basal plates (*Hoxb8*$^+$, *Stmn2*$^+$), and the olfactory epithelium (*Neurod1*$^+$, *Cldn7*$^+$). Notably, *Pitx2* (cornea), *Neurod*1 (outer layer), and *Stmn2* (inner layer) of the optic cup exhibit a gradient of expression from outer to inner layers, contributing to eye development. Conversely, in the pallium, an inverse pattern of expression was observed, likely due to the invagination process during the optic cup formation[60] (Fig. S14). The respiratory system at this stage, indicated by *Nkx2-1* and *Tbx5* expression, reveals lung-lobe and mesenchymal cells' distribution. The early motion system, including muscles, bones, and appendages, can be observed with cellular resolution from various angles, laying the groundwork for future movement and coordination. Skeletal development is marked by specific gene expressions that present the differentiation direction of cell types: *Runx2* for osteoblasts and *Col11a1* for cartilage. The digestive system begins to differentiate into the gastric and intestinal primordia, with *Cldn7* marking this early form. The circulatory system, particularly the heart, shows a clear chamber structure and atrium/ventricle differentiation (*Myl7*$^+$, *Tnnt2*$^+$), while the renal system's fine structure is delineated by *Robo2*$^+$ and *Nkx2-1*$^+$ expressions. PRISM's high resolution and accuracy effectively reveal mouse embryo's intricate structures and cell types at E13.5.

Expanding the atlas to include E12.5 and E14.5 mouse embryos offers valuable insights into their developmental progression, creating a temporal-spatial atlas with 26 whole-mount sections, 4,257,418 cells, and 107,655,795 transcripts from 30 RNAs at sub-micron resolution (Fig. 3B, Fig. S15). The period from E12.5 to E13.5 witnessed significant transformations in various tissues (muscle, skeleton, and ganglia) and organs (such as vibrissa and tongue) (Fig. 3C). By E12.5, the pancreas was identifiable as a cluster of *Spp1*-positive cells, which subsequently enlarged and underwent bifurcation by E14.5 (Fig. S16). Also, a group of *Wnt5a*$^+$ cells in the hindbrain has a significant migration behavior, suggesting morphogenic behavior of the dorsal hindbrain during development[61]. Lung development is characterized by volume reduction and increased branching and bifurcation within the lung structure (*Nkx2-1*$^+$, *Tbx5*$^+$), and a more developed trachea is observed (*Nkx2-1*$^+$). At the same time, the GI tract shows rapid development (*Cldn7*$^+$, *Tagln*$^+$), highlighting the dynamic nature of embryonic growth and organ formation.

PRISM depicts complex histological profiling of liver tumor microenvironment

We conducted a detailed analysis of a hepatitis B virus (HBV) positive hepatocellular carcinoma (HCC) sample (around 6 mm x 5 mm) using a 31-gene panel, comprising 30 selected markers associated with cell proliferation, liver tumor cells, cancer-associated fibroblasts (CAFs), endothelial cells, and immune cells, in addition to a probe targeting a 28-bp sequence encoding the HBV core protein (Fig. 4A,B, Fig. S17-19). This comprehensive panel facilitated the spatial exploration of the tumor microenvironment at single-cell resolution.

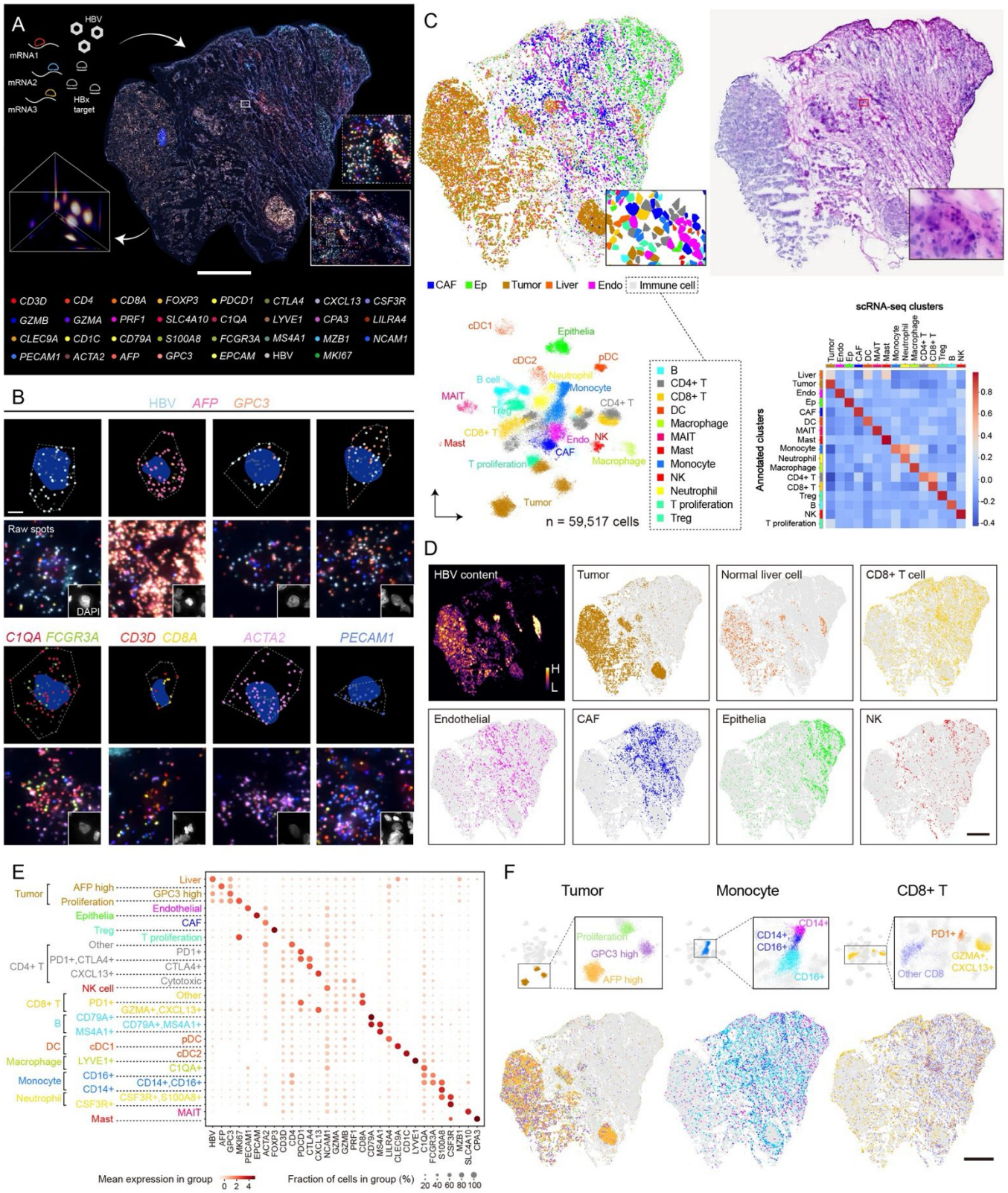

Fig. 4. Spatial profiling of human hepatocellular carcinoma cancer microenvironment by PRISM. (A) Workflow and signal results of HCC sample profiled by PRISM 31-gene panel. The panel includes 30 marker genes and an HBV core-protein-encoding RNA. Scale bar: 1mm. **(B)** Zoom-in image of called signal spot and the corresponding raw image composed of four channels and DAPI. The blue region in the first row shows the segmented nucleus and the white dot line shows the border of the segmented cell. Scale bar: 5 μm. **(C)** Cell classification in HCC sample. Left: Cell annotation result is achieved through Harmony embedding and Leiden clustering, along with the UMAP plot. Upper left: projection of all cells. Upper right: H&E staining of adjacent sample section. Lower right: Pearson correlation of PRISM cell classification results with single-cell transcriptome data. **(D)** HBV distribution and cell type projection. Scale bar: 1 mm. **(E)** Dot plot of each cell subtype. **(F)** Projection of cell subtype. Scale bar: 1 mm.

Our analysis identified 1,695,418 transcripts and assigned them to 59,517 cells, predominantly classified into 12 immune cell populations—including B cells, T cells, natural killer cells, mast cells, neutrophils, monocytes, and macrophages—and 5 non-immune cell types, such as CAFs, tumor cells, epithelial cells, endothelial cells, and normal liver cells (Fig. 4C,D, Fig. S20,21). This classification was achieved using Harmony embedding and unsupervised clustering analysis based on distinct PRISM gene marker profiles. The accuracy of cell identification by PRISM closely aligned with findings from prior single-cell RNA-sequencing studies[62–64] (Fig. 4C), validating the effectiveness of this single-round imaging technique.

By mapping single cells to their original spatial contexts, we found that the spatial distributions and positions of cells, as revealed by PRISM, well correlated with those derived from conventional fast-diagnostic hematoxylin and eosin (H&E) and immunohistochemistry (IHC) staining methods (Fig. 4C, Fig. S22). Further analysis delineated dominant cell populations into subtypes based on their unique PRISM profiles (Fig. 4E, Fig. S22-23). For instance, tumor cells were subdivided into three distinct clusters characterized by the high expression of *AFP*, *GPC3,* and *MKI67*, indicating intrinsic heterogeneity. Immune cells, such as monocytes, were further categorized into classical ($CD14^{+}CD16^{-}$), non-classical ($CD14^{dim}CD16^{+}$), and intermediate ($CD14^{+}CD16^{+}$) subtypes. Additionally, $PD\text{-}1^{+}$ exhausted and $CXCL13^{+}GZMA^{+}$ tumor-reactive CD8 T cells were identified as unique subpopulations among CD8 T cells (Fig. 4F). This nuanced classification and the investigation of spatial interactions and communications among individual cell types, especially between different subtypes, enrich our understanding of the complex dynamics within the tumor microenvironment.

Quasi-3D atlas exhibits microscale stromal heterogeneity in liver tumor

To comprehensively understand the tumor microenvironment of this HBV-infected HCC, we advanced our spatial analysis beyond simple 2D projections by constructing a quasi-3D landscape. This was achieved by stacking PRISM data from 20 consecutive tissue sections to form a thick slab-like structure (Fig. 5A). Within this structure, based on gene density, the tissue was categorized into four primary areas: tumor (Territory 1), normal liver (Territory 2), epithelia (Territory 3), and CAFs (Territory 4) (Fig. 5B).

Investigating the tumor's 3D architecture revealed its complex structural and functional characteristics, which could be oversimplified by 2D analysis alone. For instance, tumor nests appearing separate in 2D images were found to be interconnected in 3D, highlighting the intricate nature of tumor growth in complex microenvironment (Fig. 5C). The quasi-3D PRISM analysis, utilizing a 31-gene panel, maintained high consistency in cell identification with 2D and single-cell transcriptomics datasets, revealing 17 main cell clusters and identifying 1,375,952 single cells (Fig. S24). This 3D analysis more realistically represented the heterogeneity within the tumor microenvironment, showing significant variations in cell composition across the defined territories, with a predominance of tumor cells in Territory 1 and CAFs in Territory 4 (Fig. 5D).

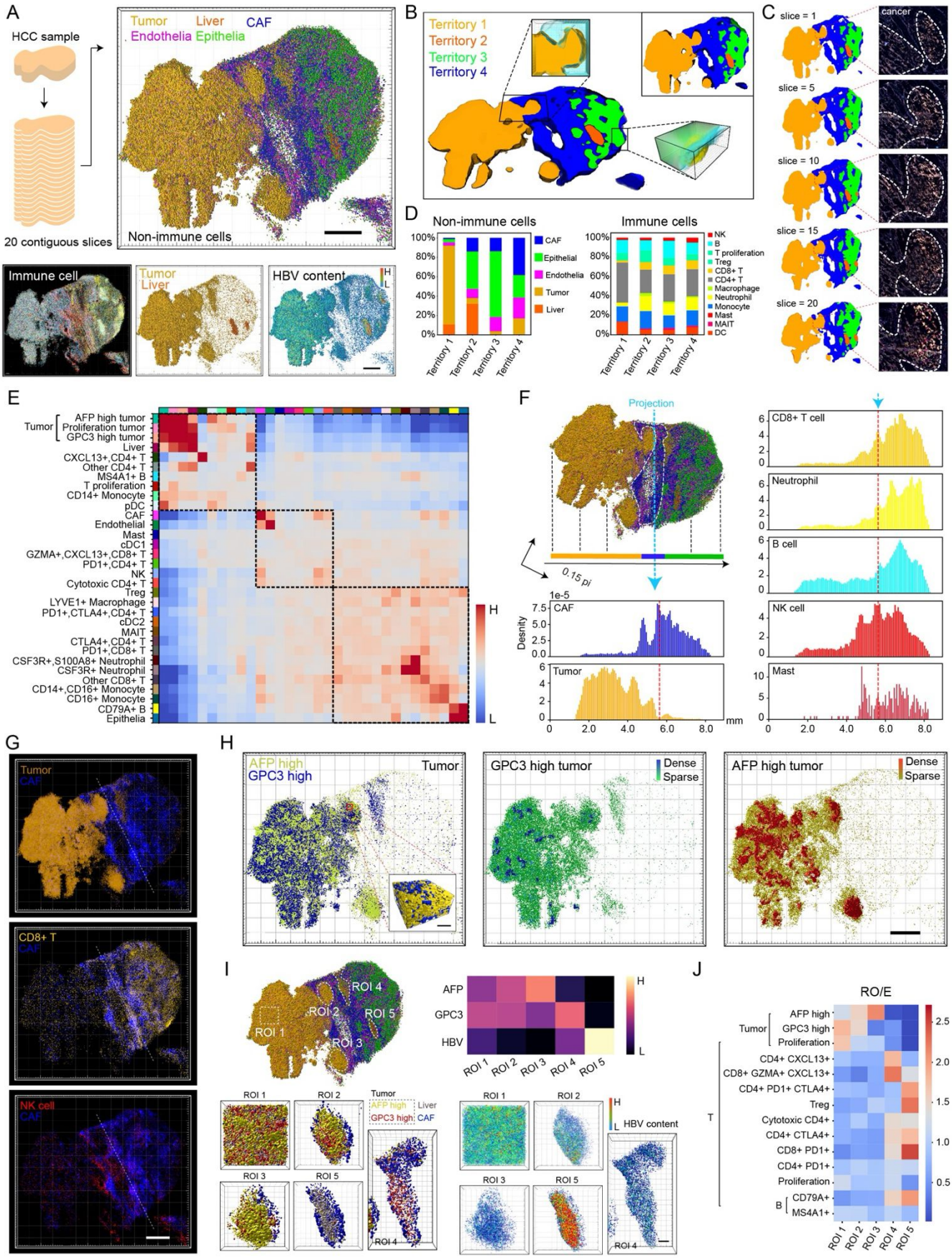

Fig. 5. Quasi-3D atlas reconstitution of HCC microenvironment through PRISM consecutive profiling. (A) reconstituted 3D cell distribution from 20 consecutive sections. Scale bar: 1 mm. **(B)** 3D territory segmented based on gene distribution: tumor (Territory 1), normal liver (Territory 2), epithelia (Territory 3), and CAFs (Territory 4). **(C)** Sections in 3D territory. The right part shows the raw image in a tumor-protrusion region. **(D)** Percentages of cells in four territories. **(E)** Neighborhood enrichment analysis for all subtypes. The enrichment value reflects the spatial correlation between cell subtypes. Three circled modules are tumor module, CAF module, and epithelia module. **(F)** CAF barrier effect on immune infiltration through cell density projection. The sample was rotated by 27˚ to align its 'long-axis' horizontally, and all cells were projected onto this long axis. The distribution histograms from several cell types

were presented. The red dot line marks the peak distribution locus of CAF. **(G)** 3D projection of CAF cells (blue color) and immune or tumor cells, displayed in the respective color. Scale bar: 1 mm. **(H)** Intra-tumor heterogeneity. On the left, GPC3-high tumor cells (blue) exhibit a more widespread distribution, whereas AFP-high tumor cells (yellow) are more localized and interconnected. The density pattern (middle and right) reflects the extent of their aggregation. The color is bluer/ redder in a denser region for the respective two subtypes. Scale bar: 100 μm, zoom-in image; 1 mm, right. **(I)** ROI analysis for the tumor and HBV-infected region. Upper left: the locations of 5 ROI. Upper right: AFP, GPC3, and HBV core-protein expression levels in 5 ROIs. Lower left: Distribution of AFP-high tumor cells, GPC3-high tumor cells, normal liver cells, and CAFs in 5 ROIs. Lower right: HBV content in 5 ROIs. Scale bar: 200 μm. **(J)** The ratio of Observed to Expected (Roe) cell type enrichment analysis in 5 ROIs.

Further analysis segmented these main clusters into 33 subpopulations based on distinct PRISM gene markers (Fig. S24). Spatial neighborhood enrichment analysis revealed three distinct cellular modules characterized by specific co-enrichment patterns: tumor, CAF, and epithelia modules, each demonstrating unique cell contexts (Fig. 5E, Fig. S25). These modules exhibited distinct cell contexts, with most immune cells located in non-tumor modules, while the tumor module displayed a lower level of immune infiltration. Notably, CAFs formed a physical barrier that restricted the infiltration of various immune cells (Fig. 5F, Fig. S26), including CD8+ T cells, macrophages, and neutrophils, into the tumor module. However, NK cells were observed to migrate across the CAF wall, appearing at the forefront of the tumor tissue, indicating their specific immune activity and anti-tumor roles (Fig. 5G).

We also explored intra-tumor heterogeneity, noting distinct spatial distributions for the HCC markers AFP and GPC3 (Fig. 5H). GPC3-high cells were evenly distributed throughout the tumor territory, whereas AFP-high cells were more localized and interconnected, suggesting subclone lineage differences. Analysis of four tumor and one normal region of interest (ROIs) revealed higher HBV core-protein expression in the normal liver tissue, suggesting early HBV expression before liver cancer development, and this sub-clone dynamic difference has high-level heterogeneity at the 100 μm scale (Fig. 5I). The immune landscape varied across these ROIs, with higher immune cell enrichment in ROI4 and ROI5, contrasting with other tumor ROIs, due to the barrier effect of CAFs (Fig. 5J). Furthermore, exhausted T cells expressing PD1 and/or CTLA4 were relatively more abundant in tumor ROI4 than in the HBV-positive normal ROI5 region. In contrast, CXCL13+ CD8 and CD4 T cells, defined as tumor-reactive T cells[65], were more enriched only in ROI4, potentially due to different immune responses against the HBV virus and tumor, respectively. This detailed investigation underscores the complex cellular interactions within HCC, offering insights that could significantly enhance our understanding of liver cancer's development and progression.

Large-scale 3D in-situ profiling unveils subcellular RNA distribution heterogeneities in intact thick tissues

We expanded the application of PRISM to analyze the intact 3D cell composition of 100-μm thick mouse brain tissue, demonstrating its inherent compatibility with the processing and imaging of thick tissues (Fig. 6A). This approach preserves the three-dimensional structure with high precision and accuracy. By employing single-round imaging, we avoid repetitive macromolecule penetration within thick tissues and effectively circumvent the challenges of fluorescent spot alignment and registration across multiple imaging sessions, which are common issues in existing multiplex RNA imaging techniques.

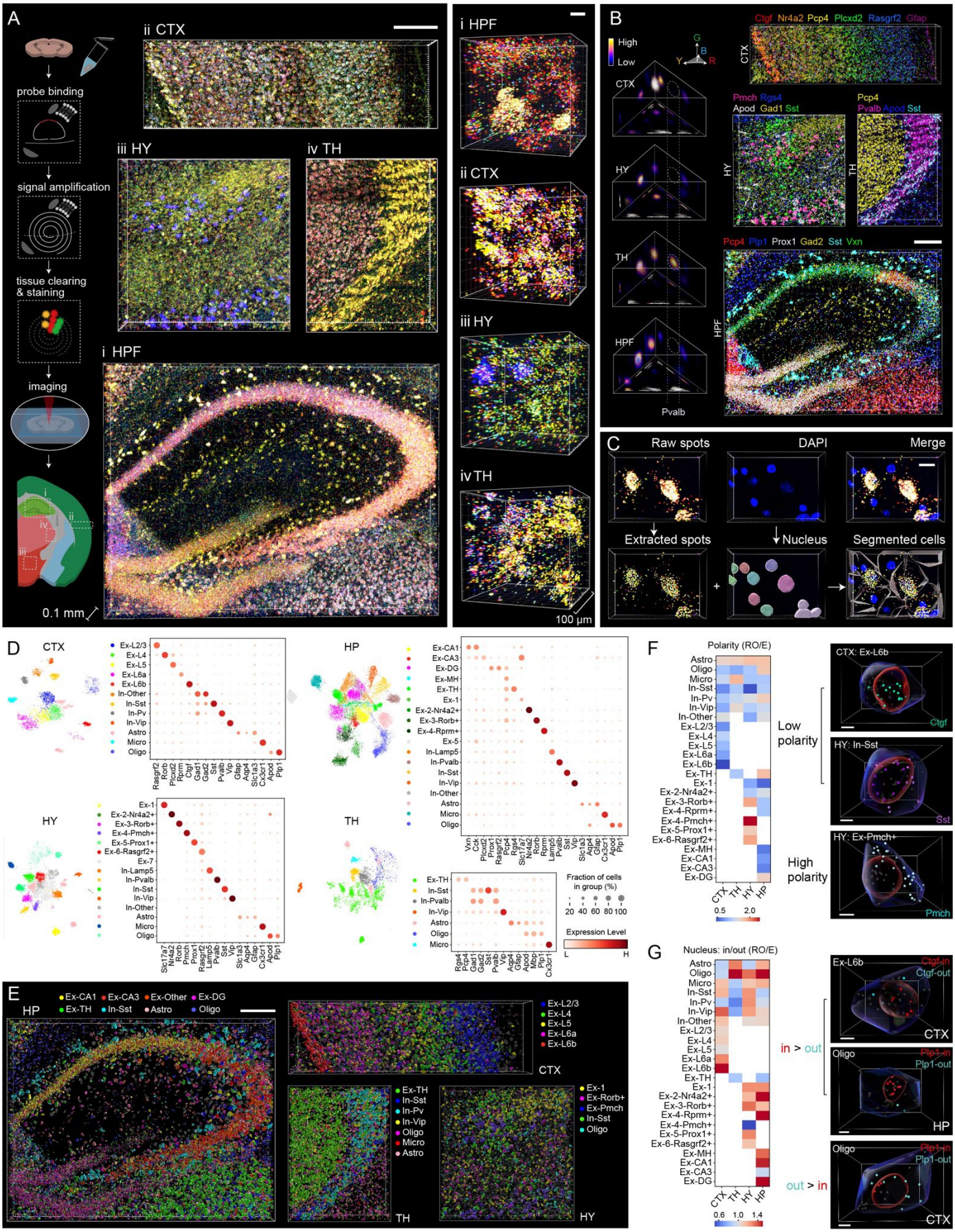

Fig. 6. Three-dimensional RNA in-situ staining in intact mouse brain tissue. (A) Workflow of PRISM 3D staining and the result. A liquid removal step is added after rolling circle amplification. RI matching was performed after fluorescent probe staining to enhance optical transparency. Resulting images depict tissues from four brain regions (HPF: hippocampus formation, CTX: cortex, HY: hypothalamus, and TH: thalamus). The images are composited using four channels (488nm, 532nm, 594nm and 647nm). Scale bar: 200 µm, upper left; 10µm, right. **(B)** Gene calling in color space for four brain tissues. The distribution of selected called genes in the

four tissues is shown on the right side. Scale bar: 200 μm. **(C)** Three-dimensional cell segmentation. Identified gene spots were assigned to nearest nucleus centroid through Euclidean distance. Scale bar: 15 μm. **(D)** Cell classification by Harmony embedding and Leiden clustering. The color of cell type is unified in UMAP plot and dot plot. **(E)** Projection of selected cell type in the four brain regions. Scale bar: 200 μm. **(F)** Subcellular RNA polarity analysis across brain regions and cell types. The polarity analysis was based on the scaled distance of RNAs' centroid and nucleus centroid within one cell. The top 20% was designated as high polarity, and the bottom 20% as low polarity. The values in heatmap were calculated through Roe analysis using the ratio of high to low polarity. Polarity values from 30 genes were averaged in each cell type. On the right: examples of cells with high / low RNA polarity. Scale bar: 5 μm. **(G)** Subcellular RNA enrichment in nucleus: this was calculated by RNA inside / outside of the nucleus. Similarly, the values were based on Roe analysis. On the right: examples of cells with RNA spots tend to distributed inside/outside of nucleus. Scale bar: 5 μm.

To improve optical transmission through thick tissues, we incorporated a post-amplification lipid-removal step and used iohexol for refractive index matching to ensure a deep light penetration (Fig. S27). PRISM decoding process utilized signal ratios rather than absolute intensities, offering greater tolerance to optical attenuation (Fig. S28). Utilizing a 30-gene panel, we profiled large-scale ROIs within the brain, including the cortex (1330 μm x 400 μm x 100 μm, 207,115 RNA transcripts), hypothalamus (770 μm x 770 μm x 100 μm, 214,671 RNAs), thalamus (585 μm x 775 μm x 100 μm, 156,368 RNAs), and hippocampus (1520 μm x 1150 μm x 100 μm, 548,220 RNAs) (Fig. 6A). The detailed morphology and distribution of marker genes within these areas align with those observed in 2D experiments, indicating consistency across dimensions (Fig. 6B).

Cell segmentation and classification within each ROI were performed using StarDist[66,67] for 3D nucleus segmentation(Fig. 6C) (resulting in 4,792 cells in the cortex ROI, 9,838 cells in the hypothalamus ROI, 5,370 cells in the thalamus ROI, and 20,721 cells in the hippocampus ROI, respectively) and Harmony embedding coupled with Leiden cell clustering, respectively, allowing for the differentiation of glial cells and neurons into subtypes (Fig. 6D). These classifications show high correlation with single-cell transcriptome data, affirming the robustness of our approach (Fig. S29). Furthermore, we projected the cells back to their original locations to construct a 3D neuron-architecture landscape (Fig. 6E).

Beyond cellular analysis, we delved into subcellular RNA distribution, assessing RNA polarity within each cell type by averaging the distances from RNA centroids to the cell centroid for each gene (Fig. 6F). This revealed notable heterogeneity in RNA polarity among neurons. For example, In-*Sst*, Ex-L6b has little polarity with given genes, but *Pmch*$^{+}$ cells in the hypothalamus display pronounced polarity, with most RNA gathering on one side of the cell body, indicative of unique cell orientations. Additionally, we explored gene enrichment within the nucleus across different cell types and brain regions, uncovering a heterogeneous RNA distribution that suggests variations in cell morphology, RNA nascency, and transcriptional activity (Fig. 6G, Fig. S30). Interestingly, the nuclear distribution may be associated with brain regions. Within the oligodendrocytes, the majority of RNA tends to distribute inside of the nucleus in the hippocampus and thalamus (mainly reflected in oligodendrocytes in fiber tracts within these two ROIs), while in the cortex, the behavior is the opposite. This subcellular RNA distribution adds another dimension to our understanding of cell types and states, enriching the comprehensive profile provided by PRISM.

Discussion

PRISM leverages radius vector coding, a method that utilizes specific spectral combinations to enhance information density within a single round of fluorescent in situ hybridization staining and imaging. This innovative approach facilitates size-independent barcoding of clonal RCA products, offering flexibility and versatility for complex tissue samples. PRISM's coding space can be

expanded by increasing the levels of division without the need to lengthen barcode sequences. This scalability is achieved by setting more divisions and reallocating each quantity of level. Each level can also be fine-tuned by adjusting the mixing ratio of fluorescent probes to non-fluorescent probes corresponding to each barcode segment in the padlock probes. This adjustability of the fluorophore proportion for each level and channel also allows for optimal differentiation in color space upon decoding, making PRISM adaptable to various optical imaging systems regardless of their specific configurations and performance characteristics.

Furthermore, considering the inherent autofluorescence of many tissues, PRISM's design accommodates quantization of each spectral channel to different levels to ensure distinguishability within a fluorescence-background environment. Demonstrated effectiveness in diverse sample types—including mouse brain, mouse embryo, and human tumor sections—and the ability to detect viral genome fragments as short as 28 bp highlight PRISM's broad applicability.

With PRISM, encoding capacity is enhanced by creating higher intensity levels within respective channels, achieving an experimentally verified encoding capability of up to 64 genes in a single imaging round using four channels (Fig. S31). Specifically, three spectral channels Ch1, Ch2, and Ch3, were quantized into fifths (0, 1/5, 2/5, 3/5, 4/5, 5/5), and the compromise channel (Ch4) was divided into three levels: high (2), low (1), and none (0). This capacity allows for detailed spatial mapping, as demonstrated in an E13.5 stage mouse embryo (Fig. S32). The information entropy of imaging is much higher in PRISM than in other multi-cycle methods. While cyclic strip-and-rehybridization methods or adding more optical channels could theoretically further increase multiplexity for PRISM, they would necessitate extensive instrumentation and image processing, compromising the ease of use. Challenges such as signal crowdedness, a common issue in amplification-based RNA in-situ detection technologies, are acknowledged as multiplexity increases. This could be addressed through expansion microscopy or introducing pseudo-channels via light-activable/switchable fluorescent dyes or fluorescence resonance energy transfer (FRET).

PRISM stands out for its cost efficiency, simplicity, and quick experimental turnaround. It utilizes standardized reagents and conventional benchtop setups, becoming a valuable tool for a wide range of applications, from molecular pathology to cell atlas construction. It reduces reliance on specialized equipment or substantial resources. With its open-source design, PRISM aims to simplify highly multiplex transcriptomic imaging, making it as accessible as standard immunostaining techniques.

Acknowledgments

The authors thank Dr. Ye Liang of the State Key Laboratory of Membrane Biology and Dr. Liqin Fu of the School of Life Sciences and National Biomedical Imaging Center at Peking University for assistance with confocal microscopy imaging. The authors thank Lei Wang for experimental assistance. This work was supported by grants from National Natural Science Foundation of China Grants 21927802 (Y.H., J.W., P.F.), T2188102 (Y.H.), T2225005 (J.W.), Beijing Municipal Science and Technology Commission Grant Z211100003321006 (Y.H.), Ministry of Science and Technology Grant 2018YFA0800200 (J.W.), and Clinical Medicine Plus X - Young Scholars Project of Peking University, the Fundamental Research Funds for the Central Universities (C.Z.).

Author contributions

Conceptualization: T.C., M.J. and Y.H. Experiment: T.C., S.Z., K.D., Z.L., M.T., Y.Z., C.Y., W.F., G.W.,

D.L., J.P., Y.P., P.F. and J.W. Data analysis: T.C., M.T., Y.Z., W.H., Z.L., S.Z., K.D., C.Z. and Y.H. Writing: T.C., S.Z., K.D., Z.L., M.T., C.Z. and Y.H.

Competing interests

Y.H., T.C., S.Z., K.D., M.T., Z.L., M.J. and W.H. have applied for a patent related to this work.

Data and Code availability

The data (raw RNA & expression matrix) and code used in the analysis are deposited in Github (https://github.com/huanglab111/PRISM_Code).

References

1. Ståhl, P. L. *et al.* Visualization and analysis of gene expression in tissue sections by spatial transcriptomics. *Science* **353**, 78–82 (2016).
2. Rodriques, S. G. *et al.* Slide-seq: A scalable technology for measuring genome-wide expression at high spatial resolution. *Science* **363**, 1463–1467 (2019).
3. Vickovic, S. *et al.* High-definition spatial transcriptomics for in situ tissue profiling. *Nat Methods* **16**, 987–990 (2019).
4. Liu, Y. *et al.* High-Spatial-Resolution Multi-Omics Sequencing via Deterministic Barcoding in Tissue. *Cell* **183**, 1665-1681.e18 (2020).
5. Lee, Y. *et al.* XYZeq: Spatially resolved single-cell RNA sequencing reveals expression heterogeneity in the tumor microenvironment. *Sci. Adv.* **7**, eabg4755 (2021).
6. Stickels, R. R. *et al.* Highly sensitive spatial transcriptomics at near-cellular resolution with Slide-seqV2. *Nat Biotechnol* **39**, 313–319 (2021).
7. Srivatsan, S. R. *et al.* Embryo-scale, single-cell spatial transcriptomics. *Science* **373**, 111–117 (2021).
8. Chen, A. *et al.* Spatiotemporal transcriptomic atlas of mouse organogenesis using DNA nanoball-patterned arrays. *Cell* **185**, 1777-1792.e21 (2022).
9. Cho, C.-S. *et al. Seq-Scope: Submicrometer-Resolution Spatial Transcriptomics for Single Cell and Subcellular Studies*. http://biorxiv.org/lookup/doi/10.1101/2021.01.25.427807 (2021) doi:10.1101/2021.01.25.427807.
10. Jiang, F. *et al.* Simultaneous profiling of spatial gene expression and chromatin accessibility during mouse brain development. *Nat Methods* **20**, 1048–1057 (2023).
11. Fu, X. *et al.* Polony gels enable amplifiable DNA stamping and spatial transcriptomics of chronic pain. *Cell* **185**, 4621-4633.e17 (2022).
12. Liu, Y. *et al.* High-plex protein and whole transcriptome co-mapping at cellular resolution with spatial CITE-seq. *Nat Biotechnol* **41**, 1405–1409 (2023).
13. Wirth, J. *et al.* Spatial transcriptomics using multiplexed deterministic barcoding in tissue. *Nat Commun* **14**, 1523 (2023).
14. McKellar, D. W. *et al.* Spatial mapping of the total transcriptome by in situ polyadenylation. *Nat Biotechnol* **41**, 513–520 (2023).
15. Russell, A. J. C. *et al.* Slide-tags enables single-nucleus barcoding for multimodal spatial genomics. *Nature* **625**, 101–109 (2024).
16. Fan, Y. *et al.* Expansion spatial transcriptomics. *Nat Methods* **20**, 1179–1182 (2023).
17. Cao, J. *et al.* Decoder-seq enhances mRNA capture efficiency in spatial RNA sequencing. *Nat Biotechnol* (2024) doi:10.1038/s41587-023-02086-y.
18. Femino, A. M., Fay, F. S., Fogarty, K. & Singer, R. H. Visualization of Single RNA Transcripts

in Situ. **280**, (1998).
19. Wang, F. *et al.* RNAscope. *The Journal of Molecular Diagnostics* **14**, 22–29 (2012).
20. Lubeck, E. & Cai, L. Single-cell systems biology by super-resolution imaging and combinatorial labeling. *Nat Methods* **9**, 743–748 (2012).
21. Lubeck, E., Coskun, A. F., Zhiyentayev, T., Ahmad, M. & Cai, L. Single-cell in situ RNA profiling by sequential hybridization. *Nat Methods* **11**, 360–361 (2014).
22. Chen, K. H., Boettiger, A. N., Moffitt, J. R., Wang, S. & Zhuang, X. Spatially resolved, highly multiplexed RNA profiling in single cells. *Science* **348**, aaa6090 (2015).
23. Shah, S., Lubeck, E., Zhou, W. & Cai, L. In Situ Transcription Profiling of Single Cells Reveals Spatial Organization of Cells in the Mouse Hippocampus. *Neuron* **92**, 342–357 (2016).
24. Codeluppi, S. *et al.* Spatial organization of the somatosensory cortex revealed by osmFISH. *Nat Methods* **15**, 932–935 (2018).
25. Eng, C.-H. L. *et al.* Transcriptome-scale super-resolved imaging in tissues by RNA seqFISH+. *Nature* **568**, 235–239 (2019).
26. Xia, C., Fan, J., Emanuel, G., Hao, J. & Zhuang, X. Spatial transcriptome profiling by MERFISH reveals subcellular RNA compartmentalization and cell cycle-dependent gene expression. *Proc. Natl. Acad. Sci. U.S.A.* **116**, 19490–19499 (2019).
27. Goh, J. J. L. *et al.* Highly specific multiplexed RNA imaging in tissues with split-FISH. *Nat Methods* **17**, 689–693 (2020).
28. Wang, Y. *et al.* EASI-FISH for thick tissue defines lateral hypothalamus spatio-molecular organization. *Cell* **184**, 6361-6377.e24 (2021).
29. Vu, T. *et al.* Spatial transcriptomics using combinatorial fluorescence spectral and lifetime encoding, imaging and analysis. *Nat Commun* **13**, 169 (2022).
30. Bugeon, S. *et al.* A transcriptomic axis predicts state modulation of cortical interneurons. *Nature* **607**, 330–338 (2022).
31. He, S. *et al.* High-plex imaging of RNA and proteins at subcellular resolution in fixed tissue by spatial molecular imaging. *Nat Biotechnol* **40**, 1794–1806 (2022).
32. Tao, Y. *et al.* Highly efficient and robust π-FISH rainbow for multiplexed in situ detection of diverse biomolecules. *Nat Commun* **14**, 443 (2023).
33. Borm, L. E. *et al.* Scalable in situ single-cell profiling by electrophoretic capture of mRNA using EEL FISH. *Nat Biotechnol* (2022) doi:10.1038/s41587-022-01455-3.
34. Fang, R. *et al. Three-Dimensional Single-Cell Transcriptome Imaging of Thick Tissues*. https://elifesciences.org/reviewed-preprints/90029v1 (2023) doi:10.7554/eLife.90029.1.
35. Hong, F. *et al.* Thermal-plex: fluidic-free, rapid sequential multiplexed imaging with DNA-encoded thermal channels. *Nat Methods* **21**, 331–341 (2024).
36. Larsson, C., Grundberg, I., Söderberg, O. & Nilsson, M. In situ detection and genotyping of individual mRNA molecules. *Nat Methods* **7**, 395–397 (2010).
37. Ke, R. *et al.* In situ sequencing for RNA analysis in preserved tissue and cells. *Nat Methods* **10**, 857–860 (2013).
38. Lee, J. H. *et al.* Highly Multiplexed Subcellular RNA Sequencing in Situ. *Science* **343**, 1360–1363 (2014).
39. Chen, X., Sun, Y.-C., Church, G. M., Lee, J. H. & Zador, A. M. Efficient in situ barcode sequencing using padlock probe-based BaristaSeq. *Nucleic Acids Research* **46**, e22–e22 (2018).
40. Deng, R. *et al.* DNA-Sequence-Encoded Rolling Circle Amplicon for Single-Cell RNA Imaging. *Chem* **4**, 1373–1386 (2018).
41. Wang, X. *et al.* Three-dimensional intact-tissue sequencing of single-cell transcriptional states.

Science **361**, eaat5691 (2018).
42. Chen, X. *et al.* High-Throughput Mapping of Long-Range Neuronal Projection Using In Situ Sequencing. *Cell* **179**, 772-786.e19 (2019).
43. Gyllborg, D. *et al.* Hybridization-based in situ sequencing (HybISS) for spatially resolved transcriptomics in human and mouse brain tissue. *Nucleic Acids Research* **48**, (2020).
44. Partel, G. *et al.* Automated identification of the mouse brain's spatial compartments from in situ sequencing data. *BMC Biol* **18**, 144 (2020).
45. Sountoulidis, A. *et al.* SCRINSHOT enables spatial mapping of cell states in tissue sections with single-cell resolution. *PLoS Biol* **18**, e3000675 (2020).
46. Alon, S. *et al.* Expansion sequencing: Spatially precise in situ transcriptomics in intact biological systems. *Science* **371**, eaax2656 (2021).
47. Liu, S. *et al.* Barcoded oligonucleotides ligated on RNA amplified for multiplexed and parallel *in situ* analyses. *Nucleic Acids Research* **49**, e58–e58 (2021).
48. Sun, Y.-C. *et al.* Integrating barcoded neuroanatomy with spatial transcriptional profiling enables identification of gene correlates of projections. *Nat Neurosci* **24**, 873–885 (2021).
49. Lee, H., Marco Salas, S., Gyllborg, D. & Nilsson, M. Direct RNA targeted in situ sequencing for transcriptomic profiling in tissue. *Sci Rep* **12**, 7976 (2022).
50. Zeng, H. *et al.* Integrative in situ mapping of single-cell transcriptional states and tissue histopathology in a mouse model of Alzheimer's disease. *Nat Neurosci* (2023) doi:10.1038/s41593-022-01251-x.
51. Ren, J. *et al.* Spatiotemporally resolved transcriptomics reveals the subcellular RNA kinetic landscape. *Nat Methods* **20**, 695–705 (2023).
52. Zeng, H. *et al.* Spatially resolved single-cell translatomics at molecular resolution. *Science* **380**, eadd3067 (2023).
53. Janesick, A. *et al.* High resolution mapping of the tumor microenvironment using integrated single-cell, spatial and in situ analysis. *Nat Commun* **14**, 8353 (2023).
54. Chang, T. *et al.* Rapid and signal crowdedness-robust in situ sequencing through hybrid block coding. *Proc. Natl. Acad. Sci. U.S.A.* **120**, e2309227120 (2023).
55. Shi, H. *et al.* Spatial atlas of the mouse central nervous system at molecular resolution. *Nature* **622**, 552–561 (2023).
56. Wu, X. *et al.* Development of Multiomics in situ Pairwise Sequencing (MiP-Seq) for Single-cell Resolution Multidimensional Spatial Omics. 2023.01.07.523058 Preprint at https://doi.org/10.1101/2023.01.07.523058 (2023).
57. Wei, L. *et al.* Super-multiplex vibrational imaging. *Nature* **544**, 465–470 (2017).
58. Zhou, T. *et al.* Spatiotemporal Characterization of Human Early Intervertebral Disc Formation at Single-Cell Resolution. *Advanced Science* **10**, 2206296 (2023).
59. Nóbrega-Pereira, S. *et al.* Postmitotic Nkx2-1 controls the migration of telencephalic interneurons by direct repression of guidance receptors. *Neuron* **59**, 733 (2008).
60. Striedter, G. F. & Northcutt, R. G. The Independent Evolution of Dorsal Pallia in Multiple Vertebrate Lineages. *Brain Behavior and Evolution* **96**, 200–211 (2021).
61. Kaiser, K. *et al.* WNT5A is transported via lipoprotein particles in the cerebrospinal fluid to regulate hindbrain morphogenesis. *Nat Commun* **10**, 1498 (2019).
62. Zhang, Q. *et al.* Landscape and Dynamics of Single Immune Cells in Hepatocellular Carcinoma. *Cell* **179**, 829-845.e20 (2019).
63. Sun, Y. *et al.* Single-cell landscape of the ecosystem in early-relapse hepatocellular carcinoma. *Cell* **184**, 404-421.e16 (2021).
64. Ma, L. *et al.* Single-cell atlas of tumor cell evolution in response to therapy in hepatocellular

carcinoma and intrahepatic cholangiocarcinoma. *Journal of Hepatology* **75**, 1397–1408 (2021).
65. Zheng, C. *et al.* Transcriptomic profiles of neoantigen-reactive T cells in human gastrointestinal cancers. *Cancer Cell* **40**, 410-423.e7 (2022).
66. Schmidt, U., Weigert, M., Broaddus, C. & Myers, G. Cell Detection with Star-Convex Polygons. in *Medical Image Computing and Computer Assisted Intervention – MICCAI 2018* (eds. Frangi, A. F., Schnabel, J. A., Davatzikos, C., Alberola-López, C. & Fichtinger, G.) vol. 11071 265–273 (Springer International Publishing, Cham, 2018).
67. Weigert, M., Schmidt, U., Haase, R., Sugawara, K. & Myers, G. Star-convex Polyhedra for 3D Object Detection and Segmentation in Microscopy. in *2020 IEEE Winter Conference on Applications of Computer Vision (WACV)* 3655–3662 (IEEE, Snowmass Village, CO, USA, 2020). doi:10.1109/WACV45572.2020.9093435.
68. Smith, K. *et al.* CIDRE: an illumination-correction method for optical microscopy. *Nat Methods* **12**, 404–406 (2015).
69. Chalfoun, J. *et al.* MIST: Accurate and Scalable Microscopy Image Stitching Tool with Stage Modeling and Error Minimization. *Sci Rep* **7**, 4988 (2017).
70. Lionnet, T. *et al.* A transgenic mouse for in vivo detection of endogenous labeled mRNA. *Nat Methods* **8**, 165–170 (2011).
71. Korsunsky, I. *et al.* Fast, sensitive and accurate integration of single-cell data with Harmony. *Nat Methods* **16**, 1289–1296 (2019).
72. McInnes, L., Healy, J., Saul, N. & Großberger, L. UMAP: Uniform Manifold Approximation and Projection. *JOSS* **3**, 861 (2018).
73. Palla, G. *et al.* Squidpy: a scalable framework for spatial omics analysis. *Nat Methods* **19**, 171–178 (2022).